International Journal of Fracture **119/120:** 387–405, 2003.
© 2003 *Kluwer Academic Publishers. Printed in the Netherlands.*

Length scales for the fracture of nanostructures

WILLIAM W. GERBERICH[1], JOHN M. JUNGK[1], MIN LI[1], ALEX A. VOLINSKY[2], JOEL W. HOEHN[3] and KARL YODER[4]
[1]*Department of Chemical Engineering and Materials Science, University of Minnesota, Minneapolis, MN 55455, U.S.A.*
[2]*Motorola Corp., Mesa AZ 85202, U.S.A.*
[3]*Seagate Technology, Bloomington, MN 55435, U.S.A.*
[4]*BioTrove, Inc., Cambridge, MA 02139, U.S.A.*

Abstract. Length scales are essential to the understanding of small volume deformation and fracture in emerging technologies. Recent analysis by two groups at the atomistic (Horstmeyer and Baskes, 1999) and mesoscopic (Gerberich et al., 2002) levels have shown the importance of the volume to surface ratio to the indentation size effect (ISE) at small depths of penetration. We have interpreted this in terms of the plastic work under the contact and the surface work associated with the creation of new surface or the excess surface stress. Treating this as a modified Griffith criterion the case is made that this same length scale should apply to the delamination of thin films. By making this simple equivalency in length scales, an R-curve analysis for crack growth resistance, G_R, in thin film delamination emerges. This recovers the classic $\sigma_{ys}^2 h/E$ term as well as the fact that interfacial toughness should scale with the square root of incremental crack growth. Here σ_{ys} is yield strength, h is thickness and E is modulus of the film. As applied to thin Cu and Au films bonded to silicon substrates, the model is in good agreement.

Key words: Delamination energy, nanoscale lengths, thin films.

1. Introduction

Current research into nanotechnology is increasingly aware of the limitations of small scales in micromachines, MEMS, microelectric interconnects and magnetic recording heads. One of these limitations is when device reliability is compromised by poor thin film adhesion. The last decade has seen a considerable effort at applying linear elastic fracture mechanics concepts toward film fracture problems (Bagchi et al., 1994; Vlassak et al., 1997; Begley et al., 2000). To a lesser extent there has been progress in understanding the elastic-plastic thin-film delamination problem particularly on the experimental side of the ledger. This is partly because of a host of possible length scale variables that can be appropriately incorporated to fit any given set of data. The confusion comes in as to how to exactly measure an appropriate length scale and as to which one(s) should be included. To illustrate the problem, we enumerate in Table 1 some of the possible length scales and evolutionary microstructural features of importance to small volume deformation and fracture. The first five parameters with asterisks are some of the possible fundamental length scales which should be considered in thin film deformation and fracture. We consider interplanar slip band spacing because of possible sub-cell structures which might evolve during a thermal-mechanical processing history. The remaining parameters can easily evolve during the deformation and fracture history, e.g. those associated with nanoindentation induced yield or fracture events.

Table 1. Possible length sacles* and evolutionary microstructural features of importance in the deformation and fracture of small volumes.

*	ℓ_s	Length of dislocation pile-up
*	ℓ_d	Distance between sources (near an indenter or in the vicinity of a crack tip)
*	ℓ_p	Interplanar spacing for slip bands
*	d	Nanocrystalline grain size
*	h	Film thickness
	h_p	Pile-up around indentation
	c	Nearest approach of $\perp$ to a crack tip
	$N_\perp$	Total number of $\perp$'s
	N_s	Number of slip bands
	$\ell_\perp$	Spacing between $\perp$'s on a slip band
	n_s	Number of $\perp$'s on a given slip band

We believe we have fortuitously arrived at a single length scale parameter that controls both small volume deformation and fracture behavior of thin films. This occurred because of two separate pathways we have been following, one dealing with the indentation size effect (ISE) in bulk crystals and one addressing delamination fracture resistance of thin films. While these seem quite disparate their commonality was that both phenomena were studied by nanoindentation. These included the ISE associated with an abrupt yield excursion in single crystals (Gerberich et al., 2002; Tymiak et al., 2001) and interfacial fracture resistance from indentation induced blister formation (Kriese et al., 1999; Volinsky et al., 1999, 2002), both of which involved small volume deformation and fracture. For a number of years now we have been drawing a parallel between the point forces associated with a crack tip and an indenter tip (Gerberich et al., 1995) and the fact that the driving forces for the two might evolve similar localized dislocation arrangements. In that paper (Gerberich et al., 1995) we also noted that the pile-up height around an indentation behaves similarly, as a function of load, for both continuum and discretized models. This further suggested that contact mechanics might provide the connective link between mesoscopic and continuum models. However, it was not until we examined the same thin film system using these two approaches that we could convince ourselves that this is truly the case and that the connective link is the length scale that controls deformation and fracture of small volumes. What we have been able to show is that with no unknown constants or parameters, the deformation length scale directly determined from a series of nanoindentations into thin films leads to an R-curve analysis for the delamination fracture resistance of those same films. This is currently shown for two Cu films of 120 nm and 3.3 μm thickness bonded with Ti to silicon wafers as well as 250 and 300 nm Au films on silicon.

2. Theoretical background

Here we consider in order some theoretical background for length scales as applied to the deformation of bulk material and the deformation and delamination of thin films, all at small scale. Specifically, we address the deformation and fracture response to nanoindentation at the nanometer scale.

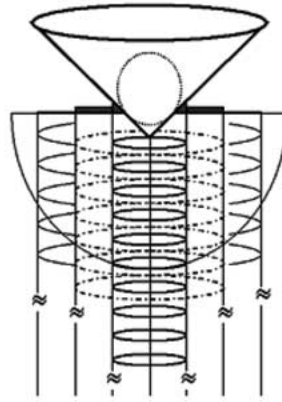

Figure 1. For the sample case of a 70 nm tip radius, the contact radius and plastic zone size are drawn to scale. The corresponding pile-up estimated from Equation (1) would be 8.8 nm representing 35 dislocation loops.

2.1. Length scale(s) for bulk deformation

Consider a conical tip with a 70 nm tip radius indenting into a surface producing concentric dislocation loops along glide cylinders. When an oxide breakthrough event occurs these travel back to the free surface resulting in pile-up as schematically shown in Figure 1. The sketched semicircle is the calculated 'elastic-plastic' boundary from continuum theory. From experimental observations of dislocation rosette patterns, we know that dislocations extend well beyond the continuum estimate. For example, from AFM profiles, we know the rosette pattern extended well beyond the pile-up region observed at the surface, measured to be 500 nm and > 3000 nm, respectively (Gerberich et al., 2001). In addition, we now know that dislocations are emitted under the tip prior to the displacement excursion and that these are released commensurate with the yield excursion. Nevertheless, the continuum theory appears to capture the essence of the plastic pile-up process.

An example of a yield excursion and the corresponding pile-ups in a ⟨100⟩Ta single crystal is shown in Figure 2. In a recent paper (Gerberich et al., 2001), the continuum representation of pile-up (Harvey et al., 1993) was found to give a good fit to plastic pile-up as determined by AFM measurement. For the contact radius, a being much smaller than the plastic zone size radius, c, plastic pile-up, h_p at the contact edge is given by

$$h_p(a) \cong (1-\nu)\frac{\sigma_{ys}}{E}\left(\frac{c^3}{a^2}\right)\frac{\pi}{2} \tag{1}$$

as formulated from Johnson's cavity model of contact mechanics (Johnson, 1970). In principal, this maximum pile-up should relate to the release of dislocations forming pile-up, as is idealized in Figure 1. Given that pile-up should be some fraction of the dislocations formed during the yield excursion, δ_{exc}, and that these to first order are δ_{exc}/b dislocations, where b is the Burger's vector, we find

$$h(a) \cong a' n_s b; \qquad \alpha' < 1 \tag{2}$$

From previous work (Gerberich et al., 2002) on the indentation size effect (ISE) we had shown that the volume to surface ratio could explain the increases in hardnesses observed at very small depths of penetration with $\delta \leq 300$ nm. The hypothesis was that the surface work was commensurate with the volume work and that this led to a constant volume (V) to surface

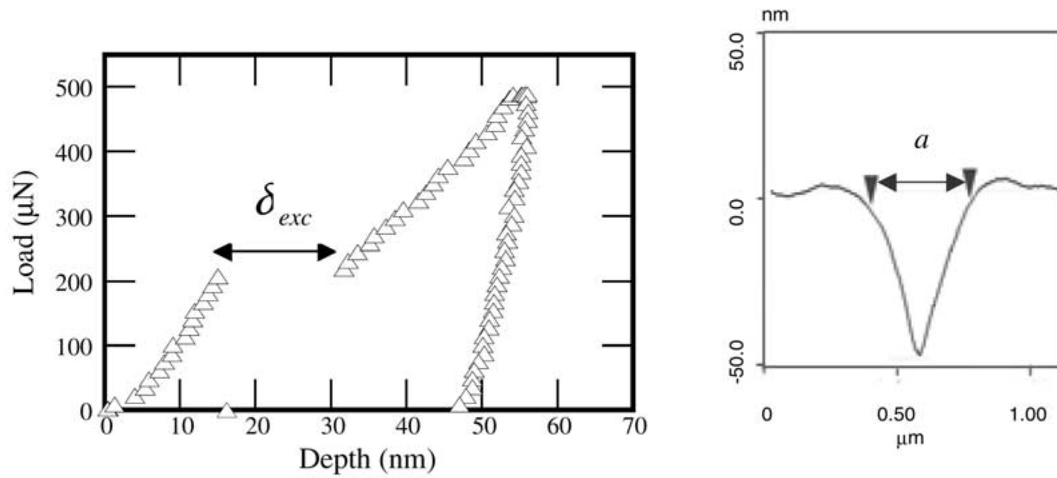

Figure 2. Yield excursion around a 1 μm radius diamond tip showing (a) displacement jump and (b) resulting pile-up measured by AFM.

ratio (S) ratio at small depths. We had previously described this plastic volume under the tip, $2\pi c^2/3$, and contact surface area, πa^2, as a length scale, ℓ_s, giving

$$\ell_s = \frac{V}{S} = \frac{2c^3}{3a^2} \tag{3}$$

in terms of the contact radius, a, and plastic zone radius, c. Furthermore, the volume work of plastic deformation $\tau_{ys}c^2\delta/2$ and the surface work $\pi a^2\gamma_s$ gave

$$\frac{W_V}{W_S} = \frac{\tau_{ys}\delta c^3}{3a^2}. \tag{4}$$

Combining (3) and (4) gives this work ratio in terms of the length scale to be

$$\frac{W_V}{W_S} = \frac{3\tau_{ys}\delta\ell_s}{4\pi\gamma_s c}. \tag{5}$$

From the data presented elsewhere (Tymiak et al., 2001) this ratio is shown for two sets of $\langle 100\rangle$ single crystal data of Al and W where three different tip radii were utilized in each case. A fourth sharpest tip for each was not considered to avoid complications of nonspherical contact. These data in Figure 3 strongly suggest that the surface work is an appreciable portion of the total work for the first several hundred nanometers of penetration. The separation of the data within each material is clearly due to the δ/c ratio with sharper tips producing a greater plastic penetration for the same plastic zone size producing a greater portion of volume work. The separation of the data between the two materials is mostly due to the yield stress to surface energy ratio with the dimensionless parameter $\tau_{ys}\ell_s/\gamma_s$ being 670 for $\langle 100\rangle$ W and 240 for $\langle 100\rangle$ Al. This further suggests that for small length scales the surface work could become extremely important as this dimensionless parameter drops below 100.

This prompted us to examine Equations (1) and (2) more closely since the plastic pile-up of Equation (1) is directly related to this length scale as it contains c^3/a^2. As we have recently discussed (Gerberich et al., 2001), the number of dislocations emitted, which then form a piled-up slip band, is obtained from Equations (1) and (2) eliminating $h(a)$ to give

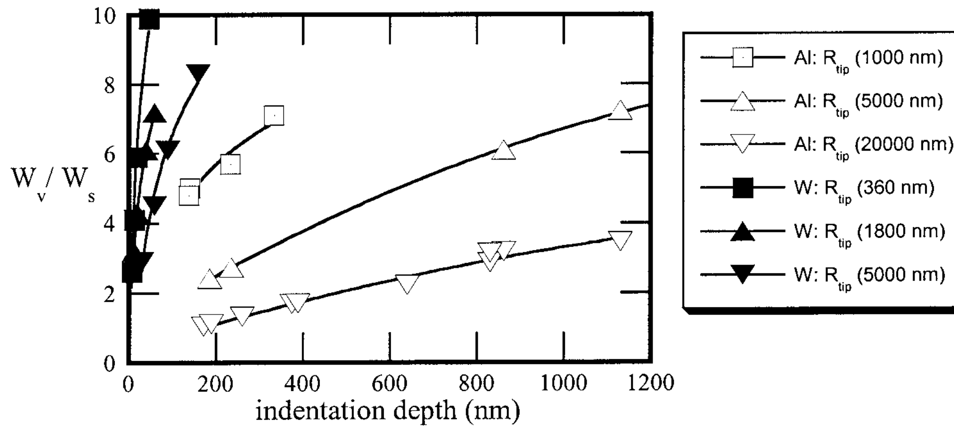

Figure 3. Volume to surface work ratio as a function of depth for a tungsten single crystal with $\ell_s \cong 4700$ nm, $\tau_{ys} = 400$ MPa and $\gamma_s = 2.8$ J m^{-2} and for an aluminum single crystal with $\ell_s \cong 7900$ nm, $\tau_{ys} = 30$ MPa and $\gamma_s = 1.0$ J m^{-2}. Indenter tip radii are those reported elsewhere (Tymiak et al., 2001).

$$n_s = \frac{\pi(1-\nu)\sigma_{ys}c^3}{2\alpha' bEa^2}. \tag{6}$$

Elimination of c^3/a^2 through Equation (3) and substituting τ_{ys}/μ for σ_{ys}/E gives

$$n_s = \frac{\pi\ell_s(1-\nu)}{2b\alpha}\frac{\tau_{ys}}{\mu} \tag{7}$$

with $\alpha = \alpha' \cdot (3/2)$. Since $\alpha' < 1$, it is tempting to take $\alpha \sim 1$ which then makes Equation (7) identical to the simple pile-up theory of Eshelby et al. (1951). The simplified picture of Figure 1 is that an inverse pile-up forms and at the yield excursion these release into the free surface causing topographical pile-up around the indenter tip. It is significant that Equation (1) is from continuum theory appropriate to the macroscale while Equation (7) is from dislocation theory appropriate to the mesoscale. This is of further interest since the original basis for Equation (3) was that for extremely small contacts into single crystals, the surface work was nearly as important as the volume work (Gerberich et al., 2002). This strongly suggests that a V/S length scale may apply equally well to the smallest of volumes that atomistically may be extremely sensitive to surface states and larger volumes that mesoscopically may be controlled by dislocation structure.

Because this appeared to work so well for small volume penetration into bulk single crystals, it was decided to apply this to the deformation of thin metal films bonded to and constrained by relatively rigid elastic substrates. Herein then lies the key. When we drastically change the size scale of the component as in thin films, how does this change the length scale(s) appropriate to deformation and fracture. As discussed above, in Table 1 we enumerated the possible length scales and a few of the evolving structural parameters that might be involved in deformation and fracture of thin films. The length scale for a thin film, clearly smaller than that for a corresponding single crystal, could be a dislocation pile-up length, a nanocrystalline grain size, d, which scales with thickness but not necessarily linearly, or film thickness, h, itself. The other parameters in Table 1 tend to be evolutionary during a point contact process and can eventually lead to friction changes, wear, film fracture or film delamination. Let us first consider definition of the V/S value for thin films as may be import-

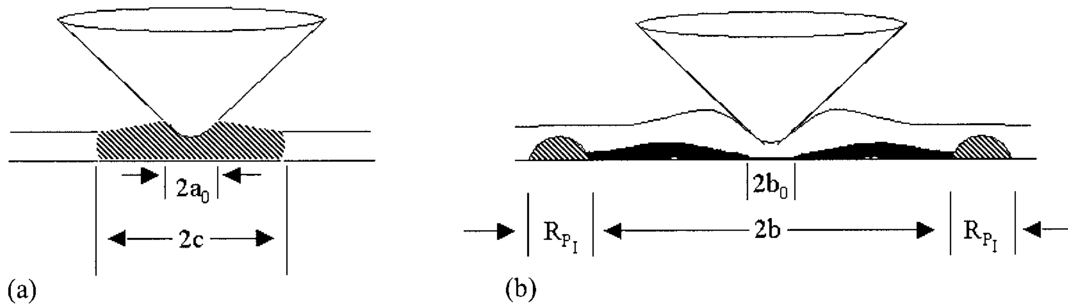

Figure 4. Plastic volumes associated with V/S for (a) a conical indenter into a constrained thin film producing a plastic zone radius of c; (b) a conical indenter producing a contact diameter of $2a_0$ producing an initial crack of $\sim 2b_0$ which grows to $2b$ under increasing load forming a plastic zone of R_{P_I}.

ant to any of these deformation and fracture processes. This is then followed by application to a film delamination process.

2.2. Length scale for thin film deformation

An in-depth series of tests (Kramer et al., 2001) for four different aluminum films of 0.34, 0.5, 1 and 2 μm thickness gave the relationship between the plastic zone size to indenter contact radius, c/a, and the normalized film thickness to be

$$\left(\frac{c}{a}\right)^2 = \frac{\alpha h}{a} \tag{8}$$

with $\alpha = 5.3$. The extent of plasticity depends on the degree of constraint and the yield stress. For smaller thicknesses, h, the substrate more easily constrains plastic flow coupling with an elevated yield stress to reduce c/a. For greater penetration and hence greater contact radii, a, the constraint factor reduces c/a. For a thin film, it is simple to translate this into a volume to surface ratio for indenters of rotational symmetry, cylinders, spheres or cones. A contact radius, a, giving a surface area of πa^2 and a constrained plastic zone, c, of $\pi c^2 h$ gives

$$\ell_s = \left.\frac{V}{S}\right|_{\text{constrained}} = \frac{\pi c^2 h}{\pi a^2}. \tag{9}$$

See the schematic of Figure 4a.

Elimination of c through (8) and (9) gives

$$\ell_s = \frac{\alpha h^2}{a}. \tag{10}$$

In reality this appears to be a mixed length scale since it depends both on the film thickness and the sharpness of the indenter which controls the contact radius for a given penetration depth. One notes that this length scale can be quite small for film thicknesses on the order of 300 nm. Since a 1 μm radius indenter penetrating to the film/substrate interface would give a contact radius of 720 nm, $\ell_s \cong 670$ nm from Equation (10), about an order of magnitude smaller than the size scale for the corresponding single crystals reported elsewhere (Gerberich et al., 2002).

2.3. Length scale application to thin film delamination

If the volume to surface ratio concept is controlled by the balance of surface work and plastic energy dissipation, clearly it is applicable to thin film delamination which can follow the modified Griffith criterion. This is schematically shown in Figures 4a and 4b for indentation and film delamination. With initial indentation only plastic deformation in a zone of length $2c$ forms as addressed above. This defines $\ell_s = V/S$. With the slightest increase of load this could trigger interface cracking at $2b_0$ which then propagates and arrests at $2b$. Now the plastic energy dissipation of importance to arrest is the deformation in the plane strain plastic zone at the advance of the crack front. We use the plane strain zone for two reasons here. First, we will apply this to films on rigid substrates where the plasticity is constrained. Second, a further constraint is provided by a superlayer of a high modulus material such as tungsten or tantalum nitride which has been applied on top of the ductile film to store elastic energy for the crack propagation process. This superlayer technique has been the subject of a number of recent investigations (Tymiak et al., 1999; Volinsky et al., 2002). This constrained plane strain plastic zone size is given by

$$R_{P_I} = \frac{K_I^2}{3\pi\sigma_{ys}^2}, \tag{11}$$

where K_I is the applied stress intensity factor. At this point the plastic volume for arrest can be assessed considering a plastic annulus of outer diameter, $b + R_{P_I}$ inner diameter b and height giving

$$V = R_{P_I}\left[\pi[b + R_{P_I}]^2 - \pi b^2 R_{P_I}\right] = 2\pi\left(bR_{P_I}^2 + R_{P_I}^2/2\right). \tag{12}$$

The corresponding surface area created by this event is the film delamination given by

$$S = \pi(b^2 - b_0^2) = \pi\left[(b_0 + \Delta b)^2 - b_0^2\right] \cong 2\pi\Delta b\left(b_0 + \frac{\Delta b}{2}\right). \tag{13}$$

From (12) and (13) we see that the ratio is

$$\frac{V}{S} = \frac{2R_{P_I}^2 b + R_{P_I}^3}{2\Delta b b_0 + \Delta b^2}. \tag{14}$$

For a number of trials using a sensible range for the incremental crack growth (blister size) and the plastic zone size we calculated V/S from Equation (14) to be

$$\frac{25R_{P_I}^2}{16\Delta b} < \ell_s < \frac{10}{3}\frac{R_{P_I}^2}{\Delta b}; \qquad 2b_0 < (\Delta b_0, R_{P_I}) < 8b_0 \tag{15}$$

which varies by about a factor of two. We are inclined toward the upper limit which represents crack-tip plastic zones smaller than the contact plastic zone. At this point we make two simplifying assumptions, one tenuous and one supported by observation. The first is that the length scale associated with plastic deformation during thin-film indentation is the same as that associated with producing crack-tip plasticity in thin films. Consider a typical thin film delamination fracture with $K_{Ic} \cong 1$ MPa m$^{1/2}$ for a 300 nm thick film having a yield strength of 500 MPa. This gives a plane strain plastic zone at the crack tip to be 420 nm from Equation (11) and compares to the 1000 nm indentation plastic zone calculated from Equation (8). Since the volume scale of these two zones is similar, we propose that the same

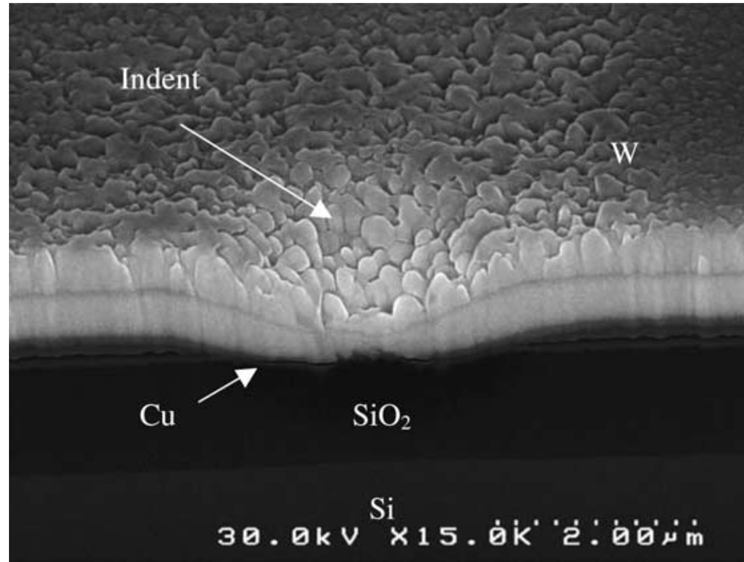

Figure 5. SEM image of the focused ion beam cross-section of a delamination in Cu film.

length scale should apply. The second assumption, as supported by observations using focused ion-beam machining (FIB) is that the contact radius just prior to delamination, a_0, is the same as the initiation defect size, b_0.

As seen in Figure 5, a FIB cross-section of a copper film delaminated from a silicon wafer shows this to be reasonable. With $\ell_s^I \sim \ell_s^c$ being the same size scale for indentation (I) and cracking (c) of these films and $a \sim b_0$ one finds from (10), (11) and the approximate upper limit of (15) that

$$\ell_s = \frac{\alpha h^2}{b_0} \cong \frac{3R_{P_I}^2}{\Delta b} \cong \frac{K_I^4}{3\pi^2\sigma_{ys}^4\Delta b}. \tag{16a}$$

From the first and fourth equalities this gives

$$K_I = \left(\pi\sqrt{3}\right)^{1/2}\sigma_{ys}\ell_s^{1/4}\Delta b^{1/4}. \tag{16b}$$

From the second and fourth equalities, this reduces to

$$K_I \cong \sigma_{ys}(\pi h)^{1/2}\left(\frac{3\alpha\Delta b}{b_0}\right)^{1/4}. \tag{16c}$$

Given that the strain energy release rate is K_I^2/E, we see that this represents a resistance curve of

$$G_R = \frac{\pi\sigma_{ys}^2 h}{E}\left(\frac{3\alpha\Delta b}{b_0}\right)^{1/2}, \tag{17a}$$

where $\Delta b/b_0$ is the ratio of incremental crack extension to the initial defect size and $\sigma_{ys}^2 h/E$ is essentially the leading term in nearly all thin film resistance models involving plasticity. This proposed R-curve behavior for forced thin film crack extension is seen to evolve directly from a simple volume to surface length scale. To recapitulate, we propose that both indentation and

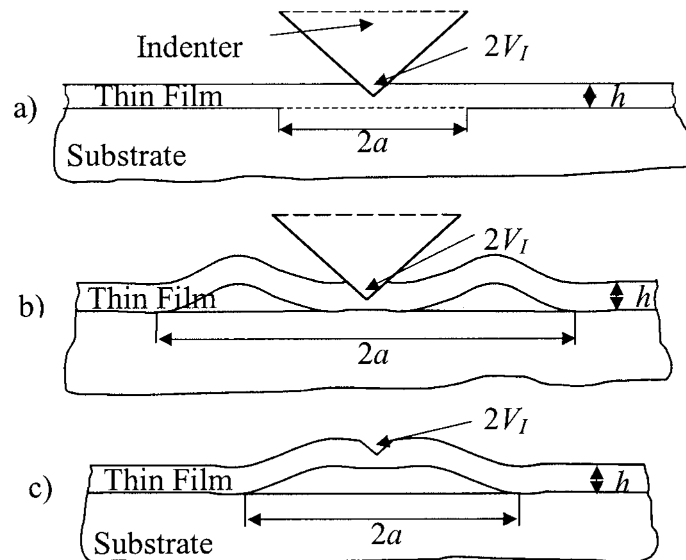

Figure 6. (a) No buckling during indentation; (b) double-buckling during indentation; (c) single-buckling after the indenter tip removal.

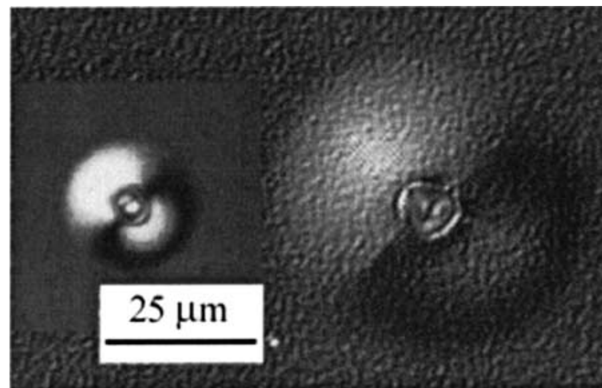

Figure 7. Optical micrographs of indentation induced blisters with (right) and without (left) a W superlayer.

fracture occurring from small volume deformation are controlled by the same length scale and that this leads to a delamination resistance criteria. Some verification of this proposed model based on existing thin film Cu and Au data follows.

3. Experimental (Cu)

A considerable amount of thin-film Cu delamination data exists as derived from superlayer indentation (Tymiak et al., 1999; Volinsky et al., 2002). A schematic of this test is shown in Figure 6. This has shown that the thin film fracture energy increases with film thickness, a result consistent with 4-pt. bend data independently determined by Lane and Dauskardt (2000). An example of the blister formed by indenting a 1 μm film of W bonded to a Cu film with a Ti underlayer between the Cu and the silicon substrate is shown in Figure 7.

At the time we noted a typical factor of three scatter in adhesion energy which we originally attributed to a b/b_0 effect different than that represented by Equation (17a). Consider then

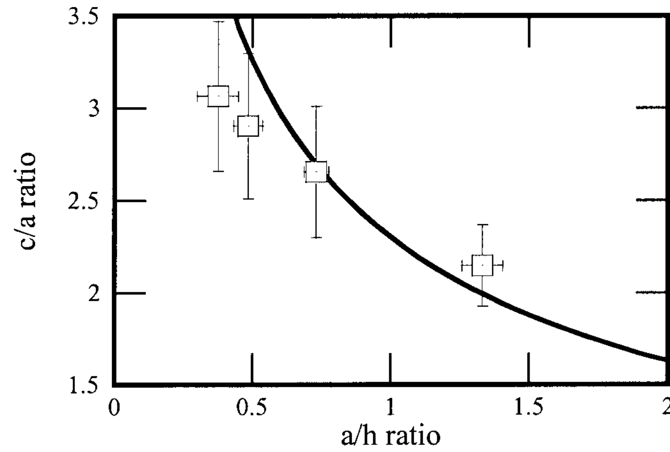

Figure 8. Fit of Equation (8) to nanoindentation produced plastic zone radii, c, normalized on contact radii, a, as a function of a/h with h being film thickness. For these Cu films, $\alpha \cong 4.8$.

the case for the same film loaded repeatedly to ever increasing loads at different indentation locations as was accomplished here. Assume the crack starts in each case when the penetration reaches a critical contact radius, say $b_0 \sim h$, since then the spherical indentation nearly reaches the interface. It is easy to see that if the penetration continues that $\Delta b/b_0$ increases and the resistance must correspondingly increase to support larger stored elastic energy release rates at higher applied loads. This is different from a purely brittle interface where a crack, once triggered, will grow and then arrest with the larger the b/b_0 the lower the fracture resistance. This latter result is obtained from the driving force side of the equation as has been derived by Marshall and Evans (1984) and Rosenfeld et al. (1990). The analysis associated with Equation (17a) concerns itself with the resistance side of the equation and what happens if further crack extension along an elastic-plastic interface beyond the initial arrest is driven by ever increasing loads. Equation (17a) is consistent with the slow crack growth observations of Au/Al_2O_3 interfaces (Lipkin et al., 1998) and remarkably similar to schematics showing resistance curves (Γ_R vs. Δa) for models based upon the embedded process zone (Evans et al., 1999).

To ascertain if such a simple length scale model can predict crack growth resistance we reexamined some Cu thin film data based on the superlayer indentation technique. For 120 nm and 3.3 μm thick Cu, data are shown in Table 2. Referring to the schematic of Figure 4, we show the corresponding values of b/b_0, penetration depth, δ, incremental crack extension, Δb, and the measured strain energy release rate from laminate composite analysis (Kriese et al., 1999). The latter is an extension of the Marshall and Evans (1984) analysis. In the tabulation for both thicknesses, it is seen that as $\Delta b/b_0$ increases, G_I generally increases. For a more quantitative comparison, it was necessary to obtain the length scale relationship as had been accomplished for aluminum films and described at Equation (10). For Cu thicknesses of 200 nm to 2000 nm deposited on Si substrates with a TiW innerlayer, we have preliminary results. For these two thicknesses, we find that the form of Equation (10) is similar with the only difference being the constant $\alpha \sim 4.8$. This is shown for one thickness in Figure 8. This gives

$$G_R = \frac{12\sigma_{ys}^2 h}{E}\left(\frac{\Delta b}{b_0}\right)^{1/2} \tag{17b}$$

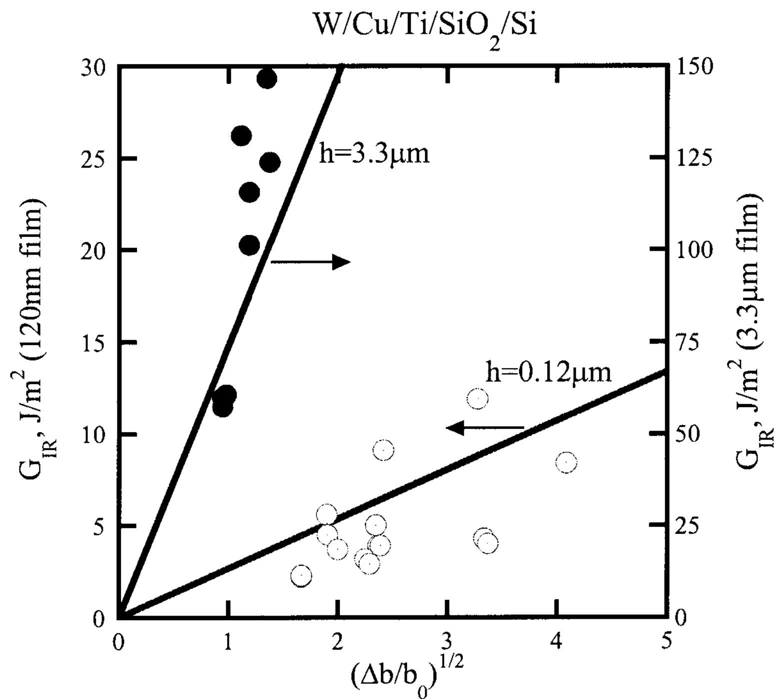

Figure 9. Crack growth resistance of Cu films as a function of incremental crack extension compared to Equation (17b).

and is seen to correspond well to the data of Table 2 reproduced in Figure 9. Here, we have used $\sigma_{ys} = 600$ MPa for the 120 nm film and $\sigma_{ys} = 460$ MPa for the 3300 nm film. Equation (17b) slightly underpredicts the thicker films and overpredicts the thinner ones in Figure 9 implying that the factor of 16 difference in toughness predicted is too small. On the other hand, using a 4-pt. bend technique, Lane and Dauskardt observed only a factor of four increase in toughness for the same increase in thickness. Note that this difference in the experimental values could be real due to differences in bond strengths giving differences in $\Delta b/b_0$ for the same film. In these two sets of data, Tymiak et al. (1999) and Volinsky et al. (2002) used a Ti bond layer while Lane and Dauskardt (2000) used a Ta/TaN bond layer between the Cu and the substrate. Furthermore, there is a degree of uncertainty about $a_0 \sim b_0$ which could easily account for any difference between prediction and observation. For these reasons we propose that this type of volume/surface approach be a serious candidate for the length scale controlling deformation and fracture of small volumes.

4. Experimental (Au)

Since extensive applicability of scratch testing has been shown for Au films with a thin DLC layer as a superlayer, we report here on preliminary results. First, it was found that indentation deformation into bare Au films with no superlayer gave a similar relationship for length scale to Equation (8) and Figure 8. In Figure 10, it is seen that Equation (8) fits the data quite well for 300 nm thick Au films with $\alpha = 15$. Considering scratch testing, we found that multiple crack initiations and arrests occurred during a single scratch. With some scatter from film to film, a good example is shown in Figure 11. One could use the maximum and minimum loads

Table 2. Indentation superlayer induced delamination of Cu films.

Cu thickness, nm	Depth, δ, nm	Delamination radius, b, nm	$(\Delta b/b_0)^{1/2}$	G_I, obs.
120	546	6800	1.67	2.2
	555	6800	1.67	2.3
	805	8400	1.91	4.5
	819	9000	2.00	3.7
	830	8300	1.90	5.6
	941	10900	2.25	3.2
	952	11200	2.29	2.9
	1067	11900	2.37	3.9
	1083	12100	2.39	3.9
	1116	11700	2.35	5.0
	1549	22300	2.42	9.1
	1869	21200	3.28	11.9
	1892	31900	4.09	8.4
	1910	22300	3.37	9.0
	1915	21900	3.34	8.95
3300	1767	6500	0.95	59.9
	1783	6700	0.985	57.3
	1811	6700	0.985	60.6
	2344	7700	1.12	131.1
	2351	8200	1.19	101.3
	2412	8200	1.19	115.6
	2818	9900	1.38	123.7
	2853	9600	1.35	146.5
	3091	10100	1.40	182

as measures of initiation and arrest. More complete data are shown in Table 3 appropriate to Figure 11. Here the contact radius, is reported in the first column of Table 3. Somewhat different in scratch testing, compared to normal indentation, is that after the first delamination event, the initial crack size, b_0, is governed by the prior delamination event. That is after the first crack initiation and arrest, we have a contact radius, a, the initial crack size where the previous event arrested, b_0, and the crack size that allows a buckling instability for the next event, b. This is schematically depicted in Figure 12 for the data in Table 3. Here it is seen that the load on the contact area, the cross-hatched region, has initially produced a delaminated region indicated by the outer dashed circle. When the contact moves to the second cross-hatched region, it is pulling on a region of the film indicated at 589 nm at the trailing edge. The crack at this stress concentration point starts growing slowly until it becomes large enough to re-initiate the delamination process, coupled with the increasing load. From the values of the maximum loads, the maximum friction coefficients, and the contact radius, a, one can first determine the normal stress and secondly the tangential stress, $\sigma_{\theta\theta}$. This is the first $\sigma_{\theta\theta}$

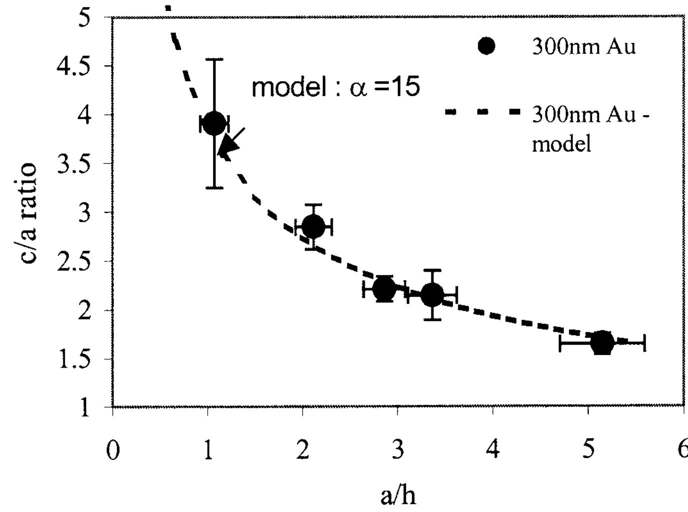

Figure 10. Nanoindentation produced plastic zone radii, c, normalized on contact radii, a, as a function of contact radii on the film thickness (a/h).

Table 3. Parameters and calculated tangential stresses and G values appropriate to sample Au12S01, $h = 250$ nm, $\sigma_{ys} = 496$ MPa.

a_0 nm	b nm	$[\sin^{-1}(a/c)]^2$	b_0[a] nm	P_L[f] μN	P_N[f] μN	σ_N GPa	μ_f[g]	$\sigma_{\theta\theta}$[b] MPa	$\sigma_{\theta\theta}$[c] MPa	G_{Ii}^{calcd} J m^{-2}	G_{Ii}[e] J m^{-2}
274	648	0.191	589	40	1060	4.49	0.519	2330	2350	8.31	10.6
303	648	0.237	589	220	1320	4.59	0.458	2100	2530	12.0	10.7
334	722	0.231	613	320	1430	4.09	0.455	1860	1650	5.55	9.1
352	759	0.233	629	380	1520	3.90	0.474	1850	1610	5.56	9.6
379	833	0.223	677	500	1640	3.55	0.442	1610	1450	4.74	7.6
399	870	0.227	702	570	1780	3.55	0.455	1615	1530	5.65	8.1
417	889	0.238	726	540	1860	3.40	0.457	1555	1670	7.73	8.1

[a] b_0 from geometric construction in Figure 12b.
[b] $\sigma_{\theta\theta}$ from normal stress times friction coefficient at initiation?
[c] $\sigma_{\theta\theta}$ from Equation (A-3).
[d] G_{Ii} from with $G_{Ii} = \frac{4\sigma_{\theta\theta}^2 b}{\pi E}\left[\sin^{-1}\left(\frac{a}{b}\right)\right]^2$ with $\sigma_{\theta\theta}$[c].
[e] Equation (A-3) except with $\sigma_{\theta\theta}$[b].
[f] P_L and P_N are lateral forces at arrest and normal force at initiation, respectively.
[g] μ_f is the friction coefficient at the local maximum load prior to each delamination event.

indicated in Table 3 and is considered to be the experimental value for each initiation event. Measuring a and b then allows a determination of both K_{Ii} and hence G_{Ii} at initiation.

Previous scratch testing of very thin films (Benjamin and Weaver, 1960; Burnett and Rickersby, 1987; Verkataraman et al., 1992, 1993), showed that delamination of Pt, Cr and Au films was possible and could lead to quantitative assessment of fracture energies. Because of uncertainties in the stress distribution at the front of an advancing stylus where the material is generally elastic-plastic, it is more appropriate to use a stress intensity approach and the furthest advance of the crack front which is more nearly elastic. This has been used by Hoehn

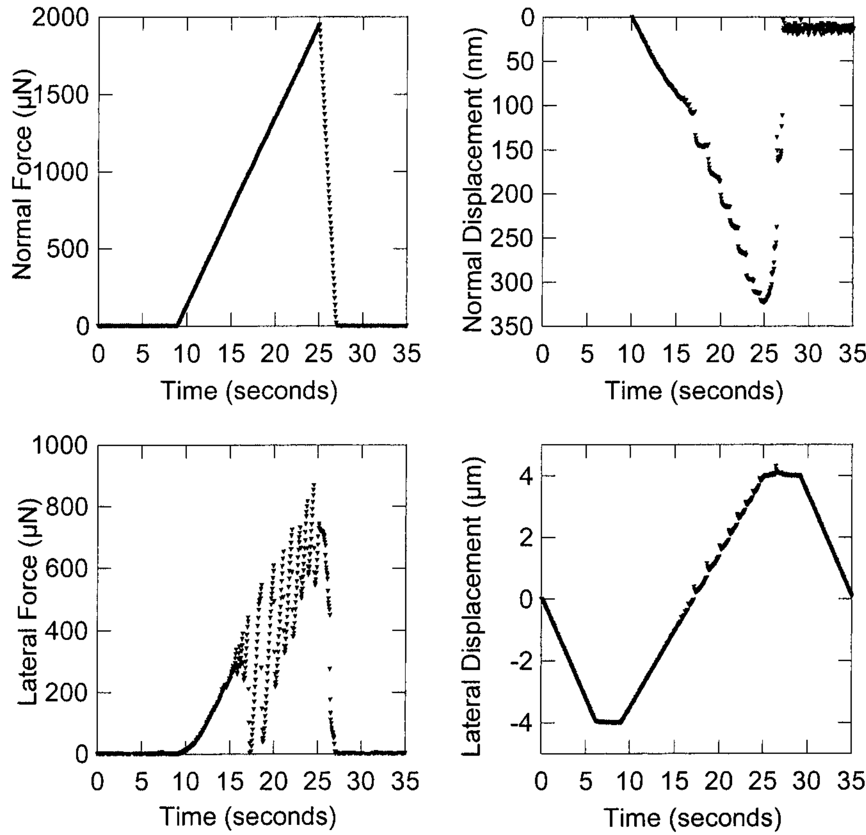

Figure 11. Raw data for sample Au12S01 showing normal (imposed) and lateral forces at the left and normal and lateral displacements to the right. The forces are in μN while the displacements are in nm (top) and μm (bottom).

et al. (1995) for scratch analysis of relatively brittle bulk materials and Turner and Evans (1989), for delamination of thin films. Knowing the contact radius, a, and the half-crack, c, associated with delamination/buckling extending from the contact, one can calculate the stress intensity from

$$K_I = 2\sigma_{\theta\theta}\sqrt{\frac{b}{\pi}}\sin^{-1}\left(\frac{a}{b}\right), \tag{18}$$

where $\sigma_{\theta\theta}$ is the tangential stress that can be defined by a lateral force transducer of the friction coefficient times the normal stress, $\mu\sigma_N$. Note here that the scratch track width, $2a$, can be defined by geometry. For the approximate 90° cone with a spherical tip of this study, the tip area function was experimentally determined to be

$$A_{\text{tip}} = 3.866 + 1.516 \times 10^3\delta + 3.319 \times 10^{-2}\delta^2 + 2.509 \times 10^{-3}\delta^3 \tag{19}$$

in nm^2 units. Here, δ is the vertical displacement of the tip into the surface in nm. Because of the circular shape of the contact, this then allowed the contact radius, a, to be determined from $\sqrt{A/\pi}$. With the extent of delamination, $2b$, defined by friction force (deflection mode AFM) microscopy, all parameters are known to determine K_I from Equation (18).

With the first column of $\sigma_{\theta\theta}$ values in Table 3, G_{Ii}, was determined. Similarly, the value of G_{IA}, the strain energy release rate at arrest, was determined using the lateral force at arrest

in column five of Table 3 to define $\sigma_{\theta\theta}$ at arrest. These values on initiation and arrest were compared to theoretical estimates determined in the following way. For arrest, we initially attempted to use the theoretical resistance, G_R, from Equation (17a) knowing that the yield strength of this 250 nm Au film was 496 MPa. One assumption was that the length scale constant, α, for the 300 nm Au film of Figure 10 was also appropriate to the data of Figure 11. However, the agreement of G_{IA} at arrest and G_R from Equation (17a) was poor. We reasoned that the major difference between the Au and Cu data was that a 1 μm superlayer of W on the Cu films did not compare to the 70 nm diamond like carbon superlayer on Au. Whereas plane strain was assumed for Cu, the thinner DLC on the Au films made the latter more nearly plane stress. With that being the case, the 3 in Equation (17a) disappears and with $\alpha = 15$, this becomes

$$G_R = \frac{12.2\sigma_{ys}^2 h}{E}\left(\frac{\Delta b}{b_0}\right)^{1/2} \tag{17c}$$

not too different from Equation (17b).

A similar analysis was conducted for the initiation value, G_{Ii}, in terms of the resistance of the side ligaments indicated by the shaded regions of Figure 12. This is detailed in the Appendix. In terms of the side-ligament yield behavior, the tangential stress $\sigma_{\theta\theta}$ shown in Table 3 agrees reasonably well with the tangential stress determined directly from the normal stress and the friction coefficient. With no adjustable constant (we take $\beta = 1$), the theoretical estimate for initiation is calculated from $\sigma_{\theta\theta}$ and Equation (18). The comparison shown in Figure 13 is reasonably consistent with at least some expectations. First for arrest, the R-curve prediction is quite good and demonstrates that the greater amount of slow crack growth required increases the resistance at large values of b_0. That is the toughness at arrest increases along the scratch track. On the other hand, the increasing contact area compensates for the increased lateral force at initiation with the resulting values of G_{Ii}, being nearly constant or slightly decreasing along the scratch track. The result appears to be that while G_{Ii} is nearly constant, the value of G_{IA} or G_R for the crack arrest condition increases quite rapidly. As a result, these two values tend to converge being separated by no more than a factor of two toward the end of the scratch.

5. Summary

We have first shown a connectivity between mesoscopic and macroscopic deformation theories through plastic pile-up around a nanoindenter. This recovers the classic dislocation pile-up model of Eshelby et al. (1951). To achieve this, a volume (V) to surface (S) ratio model has been invoked, previously shown (Gerberich et al., 2002; Tymiak et al., 2001) to predict the indentation size effect (ISE) at small penetration depths. The length scale, $\ell_s = V/S$ has then been shown to apply to both small volume deformation and fracture through nanoindentation studies of thin film copper and gold bonded to silicon substrates. This produces a fracture toughness which is proportional to the fourth root of the length scale or, alternatively, a resistance curve with the resistance proportional to the square root of the incremental crack growth. With increasing crack growth it is shown that Cu bonded to silicon substrates with a thin Ti layer increases its fracture resistance by a factor of three.

The R-curve behavior for crack arrest is shown to apply to Cu films 120 and 3300 nm thick and Au films 250 nm thick. In the former fracture was by the superlayer indentation technique while in the latter it was by the superlayer scratch test. Also shown with the scratch test is that

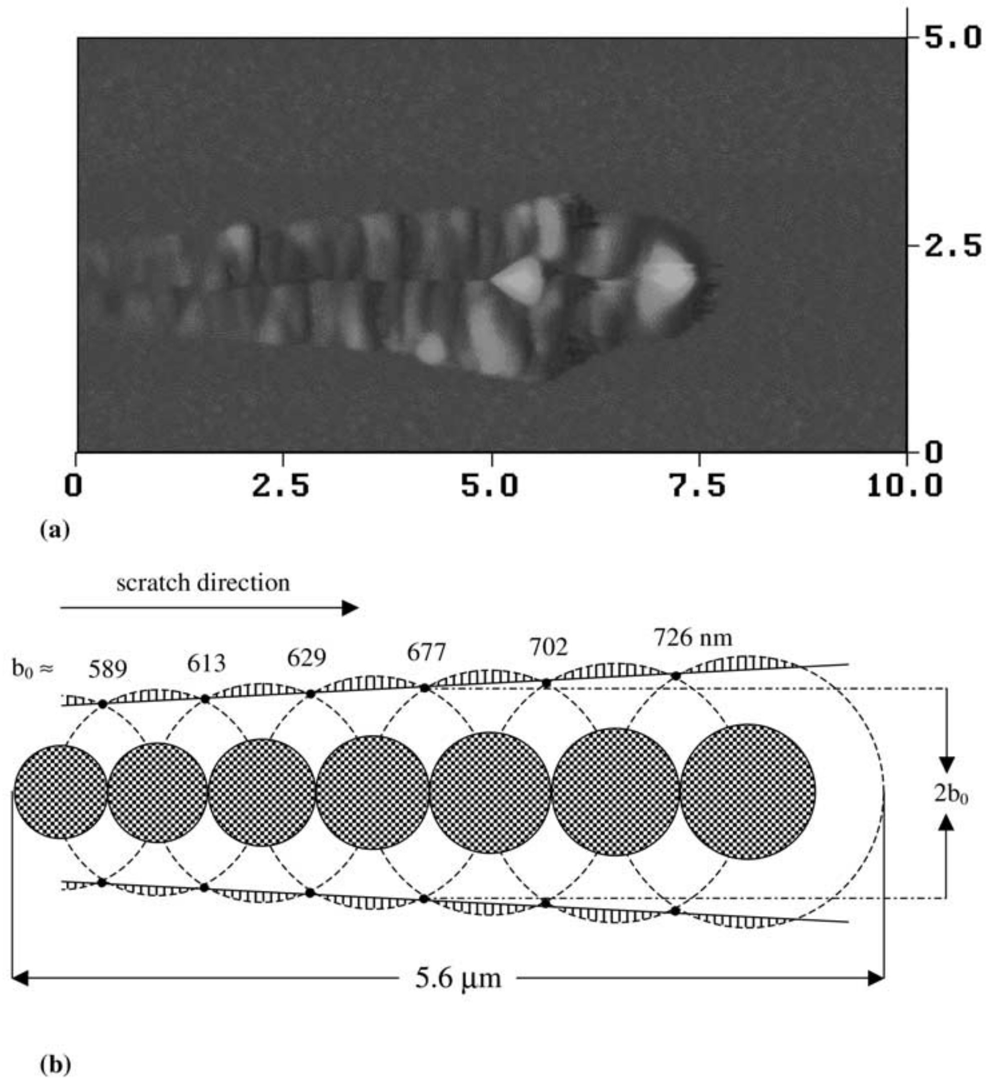

Figure 12. (a) Scratch track in 250 nm Au film showing multiple buckle delaminations (b) schematic showing local instabilities resulting in crack propagation at increasing values of b_0.

multiple values of initiation and arrest may be determined with the values tending to converge as the scratch track lengthens.

Acknowledgements

The authors would like to acknowledge support through MINT (The Center for Micromagnetics and Information Technology) via Seagate Technology, Motorola, Inc., and the Department of Energy under DOE contract DE-FG02/96ER45574. We would also like to thank Indira S. Adhihetty, Joseph B. Vella, Robert H. Carpenter and Lester Casoose Jr. of Motorola, Inc. for help with the FIB analysis.

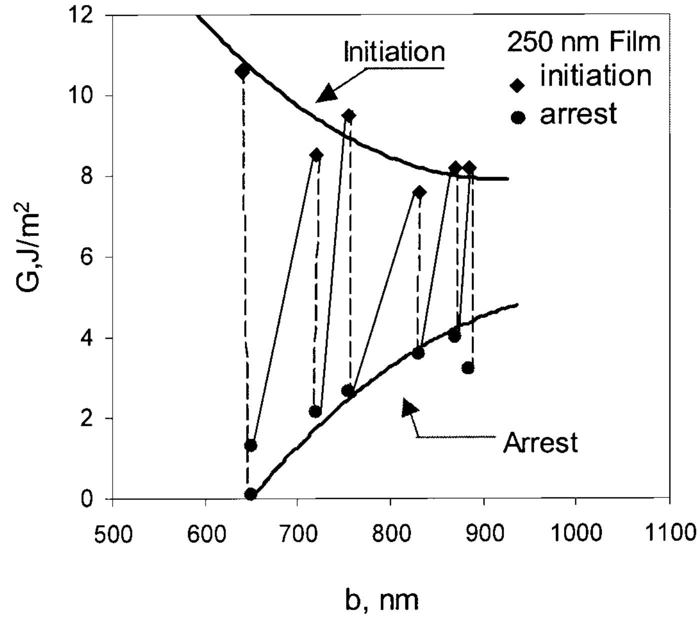

Figure 13. Initiation and arrest energies for Au12S01 as a function of delamination radius along the scratch track. Solid curves are based upon Equations (18) and (A-3) for $\sigma_{\theta\theta}$ at initiation and Equation (17c) for arrest.

Appendix: Determination of $\sigma_{\theta\theta}^{\mathrm{calc}}$

Here, $\sigma_{\theta\theta}$ as used in calculations for Table 3 is $\mu_f \sigma_N$ where σ_N is defined as the normal force divided by contact area πa^2 and μ_f is the measured friction coefficient. But the resistance to lateral force is the vertical shaded region beyond the contact in Figure 12b that is being required to grow prior to the next instability. We call this contact area the resistance to continued crack growth. A measure of this resistance is the increased crack area which will form times the thickness of the thin film, $2(b-b_0)h$, as indicated at a given point of crack advance by one of the vertical shaded bars in Figure 12b. When this reaches a maximum in the shaded region or the outside extremities of the dashed region, the next buckling instability curve occurs. To first order we propose that the lateral force divided by this maximum uncracked ligament area, A_ℓ, is proportional to $\sigma_{\theta\theta}$, as given by

$$\sigma_{\theta\theta} = \frac{\beta_2 \mu_f P_N}{A_\ell}, \tag{A-1}$$

where β_2 is some constant near unity.

In terms of a crack growth advance at this buckling instability, rather than using the measured normal load, we assume the normal load is proportional to the contact area times the film yield strength giving

$$P_N = \beta_1 \sigma_{ys} \pi a^2 \tag{A-2}$$

where β_1 a some constant near unity.

We can thus describe the $\sigma_{\theta\theta}$, tangential stress, from (A-1) and (A-2) to be

$$\sigma_{\theta\theta} = \frac{\beta \mu_f \sigma_{ys} \pi a^2}{2(c - c_0)h} \tag{A-3}$$

with $\beta = \beta_1\beta_2 \approx 1.14$.

Knowing that the yield strength of sputter deposited Au films could be given by (Volinsky et al., 2002)

$$\sigma_{ys} = \sigma_{\text{Au}}\left[1 + \beta_{\text{Au}}h^{-1/2}\right] \tag{A-4}$$

with $\sigma_{\text{Au}} = 315$ MPa and $\beta_{\text{Au}} = 0.287\ \mu\text{m}^{1/2}$, we determined the yield strength to be 496 MPa for the 250 nm thick film. This allowed us to calculate $\sigma_{\theta\theta}$ from Figure 12 which assumes contact regions (the cross-hatched areas) to trigger the sequential series of load drops seen in Figure 11. With values of b_0 from the geometrical construct in Figure 12b, the values of a from the tip area function, and values of b from atomic force microscopy, everything was available for calculating $\sigma_{\theta\theta}$ from Equation (A-3). These and other values as discussed in the text are reported in Table 3. The friction coefficient reported came directly from the transducer output of P_L/P_N, the lateral and normal forces at the initiation (local maximum) of each event in Figure 11.

References

Bagchi, A., Lucas, G., Suo, Z. and Evans, A. (1994). A new procedure for measuring the decohesion energy for thin ductile films on substrates. *J. Mater. Res.* **9**(7), 1734.

Begley, M.R., Mumm, D.R., Evans, A.G. and Hutchinson, J.W. (2000). Analysis of a wedge impression test for measuring the interface toughness between films/coatings and ductile substrates. *Acta Mater.* **48**, 3211.

Benjamin, P. and Weaver, C. (1960). Measurement of adhesion of thin films. *Proc. Roy. Soc. London* **A254**, 163.

Burnett, P. and Rickersby, D. (1987). Relationship between hardness and scratch adhesion. *Thin Solid Films* **154**, 403.

Eshelby, J.D., Frank, F.C. and Nabarro, F.R.N. (1951). The equilibrium of linear arrays of dislocations. *Philos. Mag.* **42**, 351.

Evans, A.G., Hutchinson, J.W. and Wei, Y. (1999). Interface adhesion: effects of plasticity and segregation. *Acta Mater.* **47**(15), 4093.

Gerberich, W.W., Tymiak, N.I., Grunlan, J.C., Horstemeyer, M.F. and Baskes, M.I. (2002). Interpretations of indentation size effects. *J. Appl. Mech.* **69**, 433.

Gerberich, W.W., Tymiak, N.I., Kramer, D.E., Daugela, A., Jungk, J. and Li, M. (2002). An approach to dry friction and wear for small volumes. *Philos. Mag. A*, **82**, 3349.

Gerberich, W.W., Lilleodden, E.T., Foecke, T.J. and Wyrobek, T.J. (1995). Dislocation Mechanics of Point Forces. *Micromechanics of Advanced Materials*. J.C.M. Li Symposium, TMS, Warrendale, PA, 29–35.

Harvey, S., Huang, H., Venkataraman, S. and Gerberich, W.W., (1993). Microscopy and microindentation mechanics of single crystal Fe - 3 wt. % Si: Part I. Atomic force microscopy of a small indentation. *J. Mater. Res.* **8**(6), 1291.

Hoehn, J.W., Venkataraman, S.K., Huang, H. and Gerberich, W.W. (1995). Micromechanical toughness test applied to NiAI. *Matl's. Sci. and Engng.* **A192/193**, 306.

Horstemeyer, M.E. and Baskes, M.I. (1999). Atomistic finite deformation simulations: a discussion on length scale effects in relation to mechanical stresses. *J. Engng. Mater. Tech., Trans. ASME* **121**, 114.

Johnson, K.L. (1970). The correlation of indentation experiments. *J. Mech. Phys. Solids* **18**, 115.

Kramer, D.E., Volinsky, A.A., Moody, N.R. and Gerberich, W.W. (2001). Substrate effects on indentation plastic zone development in thin soft films. *J. Mater. Res.* **16**(11), 3150.

Kriese, M.D., Moody, N.R. and Gerberich, W.W. (1999). Quantative adhesion measures of multilayer films – I. Indentation mechanics, II. Indentation of W/Cu, W/W, Cr/W. *J. Mater. Res.* **14**(7), 3007 (Part I), 3019 (Part II).

Lane, M. and Dauskardt, R.H. (2000). Adhesion and reliability of copper interconnects with Ta and TaN barrier layers. *J. Mater. Res.* **15**(1), 203.

Lipkin, D.M., Clarke, D.R. and Evans, A.G. (1998). Effect of interfacial carbon on adhesion and toughness of gold-sapphire interfaces. *Acta Mater.* **46**(13), 4835.

Marshall, D.B. and Evans, A.G. (1984). Measurement of adherence of residually stressed thin films by indentation. I. Mechanics of interface delamination. *J. Appl. Phys.* **56**, 2632.

Ostertag, C.P., Charalambides, P.G. and Evans, A.G. (1989). Observations and analysis of sintering damage. *Acta Metall.* **37**(7), 2077.

Rosenfeld, L.G., Ritter, J.E., Lardner, T.J. and Lin, M.R. (1990). Use of the microindentation technique for determining interfacial fracture energy. *J. Appl. Phys.* **67**(7), 3291.

Tymiak, N.I., Kramer, D.E., Bahr, D.F., Wyrobek, T.J. and Gerberich, W.W. (2001). Plastic strain and strain gradients at very small indentation depths. *Acta Mater.* **49**, 1021.

Tymiak, N.I., Volinksy, A.A., Kriese, M.D., Downs, S.A. and Gerberich, W.W. (1999). The role of plasticity in bimaterial fracture with ductile interlayers. *Metall. Mater. Trans.* **31A**, 863.

Venkataraman, S., Kohlstedt, D. and Gerberich, W.W. (1993). Continuous microindentation of passivating surfaces. *J. Mater. Res.* **8**, 685.

Venkataraman, S., Kohlstedt, D. and Gerberich, W.W. (1992). Microscratch analysis of the work of adhesion for Pt thin films on NiO. *J. Mater. Res.* **7**, 1126.

Vlassak, J.J., Drory, M.D. and Nix, W.D. (1997). A simple technique for measuring the adhesion of brittle films to ductile substrates with application to diamond-coated titanium. *J. Mater. Res.* **12**, 1900.

Volinksy, A.A., Moody, N.R. and Gerberich, W.W. (2002). Interfacial toughness measurements for thin films on substrates. *Acta Mater.* **50**, 441.

Volinksy, A.A., Tymiak, N.I., Kriese, M.D., Gerberich, W.W. and Hutchinson, J.W. (1999). Quantitative modeling and measurement of copper thin film adhesion. *Mater. Res. Soc. Proc.* **539**, 277.